De-blurring of frequency-wavenumber images from small-scale seismic arrays.

M. Picozzi[(1)], S. Parolai[(1)], D. Bindi[(2)].

(1) Helmholtz Centre Potsdam GFZ German Research Centre for Geosciences, Germany, (2) Istituto Nazionale di Geofisica e Vulcanologia, via Bassini 15, 20133 Milano, Italy.

Abstract

Temporary arrays installed in urban areas for investigating the upper-most geological structure typically comprised of a limited number of stations and are arranged in geometries constrained by environmental boundaries. Therefore, it is expected that the frequency-wavenumber images are significantly blurred by the array transfer function and are corrupted by noise.

In this paper, the effect of the Richardson-Lucy regularization method applied to the problem of de-blurring frequency-wavenumber images is investigated. The images are computed by analyzing data from two small-aperture 2D-arrays, installed with different configurations in a test-site within the town of Potenza (Southern Italy) for near-surface investigations. We show that removing the effects of the array response from the frequency-wavenumber images improves the phase-velocity estimation, reducing the relevant level of uncertainty. Furthermore, the Richardson-Lucy regularization method is effective in reducing the level of noise related to spatial aliasing by eliminating spurious peaks, allowing the maxima related to different seismic sources to be better discriminated.

Acronyms

ARF – Array Response Function
BFM – Beam Forming Method
MLM – Maximum Likelihood Method
TR – Tihkonov Regularization
RLM – Richardson-Lucy Method
PSF - Point-Spread Function
f-k PSDF – frequency-wavenumber Power Spectrum Density Function

1. Introduction

Seismic arrays were originally proposed at the beginning of the 1960s as a new type of seismological tool for the detection and identification of nuclear explosions (e.g. Frosch and Green, 1966). Since then, seismic arrays have been applied at various spatial scales for many geophysical purposes. At the regional scale, they have been used to obtain refined velocity models of the Earth's interior (e.g., Birtill and Whiteway, 1965; Whiteway, 1966; Kárason and van der Hilst, 2001; Ritter et al., 2001; Krűger et al., 2001). Recent reviews on array applications in seismology can be found in Douglas (2002) and Rost and Thomas (2002 and 2009).

At smaller scales (i.e. maximum aperture of the array is of the order of about one hundred meters), following the pioneering work of Aki (1957), seismic arrays have been used for the characterization of surface-wave propagation, and the extraction of information about the shallow subsoil structure (i.e. the estimation of the local S-wave velocity profile). Especially in the last decades, due to the focus of seismologists and engineers on estimating the amplification of earthquake ground motion as a function of local geology, and the improvements in the quality and computing power of instrumentation, interest in analyzing seismic noise recorded by arrays (e.g. Horike, 1985; Hough et al., 1992; Ohori et al., 2002; Okada, 2003; Scherbaum et al. 2003, Parolai et al., 2005) has grown.

Frequency-wavenumber analysis (*f-k*) (Capon et al., 1967; Capon, 1969; Lacoss et al., 1969) is one of the most important and commonly used techniques for the analysis of seismic signals recorded by arrays at both small and large scales. The basic operation for *f-k* analysis is the estimation of the frequency-wavenumber power spectral density function (*f-k PSDF*), since it provides information about the frequency composition, mode structure and properties of the seismic waves traveling across the array.

However, the accuracy and resolution in the estimation of the *f-k PSDF* strongly depends on the spatial sampling of the ground movement made by the array. In fact, similarly to the effect occurring when sampling a signal in the time domain, a non-adequate wavefield spatial sampling may be the cause of aliasing effects in the wavenumber domain.

Despite extensive seismological literature dealing with the theory of array characteristics and configurations (e.g. Carpenter, 1965; Somers and Manchee, 1966; Haubrich, 1968; Harjes and Henger, 1973; Mykkeltveit et al., 1983; Kind et al., 2005; Wathelet et al., 2005), only a few qualitative suggestions have been made regarding the improvement of *f-k PSDF* estimation. In fact, since Haubrich (1968), it has been simply recommended to choose, for a fixed number of sensors, those array configurations that guarantee the irregular sampling of both small and large wavelengths. On the other hand, there is no ideal outline for an array's configuration, since every configuration has both advantages and disadvantages over other types. Hence, for the seismological community, the solution of all the *f-k PSDF* accuracy and resolution problems has been based essentially on the selection of a particular array configuration by a visual, check of the array transfer function characteristics (see, among many others, Halldorsson et al. 2009). For instance, Wathelet et al. (2005) suggested to identify the maximum usable wavenumber by directly picking the major aliasing peaks within the array

transfer function, while the minimum wavenumber can be approximately deduced by considering the width of the central peak.

In analogy with the correction for the sensor impulse response applied before analyzing any seismic recording, in this work we propose to correct the *f-k* PSDF estimate for the effects introduced by the array transfer function. To our knowledge, in seismology, only Nishida et al. (2008), who studied the Earth's background free oscillations using the Hi-net tiltmeter network (some hundreds of sensors) while focusing on the very low frequency range (i.e. 0.01 to 0.1 Hz), deconvolved the *f-k* images before analyzing them.

The array transfer function is determined by the array geometry. Differently from the case of dense permanent networks (Nishida et al., 2008), the transfer functions of arrays with a limited number of stations (of the order of 10 to 20 for near-surface investigations) generate significant blurring in the *f-k PSDF*. Moreover, over our frequency range of interest (generally >1Hz), the background noise is generated locally by anthropic sources that can change rapidly over time. It follows, therefore, that the nature of a seismic noise wavefield over this frequency range leads to *f-k* images more corrupted by incoherent patterns than in the case of low-frequency seismic noise. These patterns, which can be thought of as noise corrupting the blurred image, could be strongly amplified by the deconvolution for the array response. Therefore, it follows that choosing the regularization approach adopted for near-surface applications might not be as straightforward as in the case of dense arrays, and may play a very critical role. In this work, we investigate the effects of removing the array response function from the *f-k* PSDF estimated by applying either the Beam-Forming Method (BFM) (Lacoss et al. 1969) or the Maximum Likelihood Method (MLM) (Capon, 1969). Two different algorithms are considered to regularize the deconvolution, namely the Richardson-Lucy and the Tikhonov methods (Bertero and Boccacci, 1998).
This paper is organized as follows. We first provide an overview of the basic concepts of both the *f-k* analysis and of the tested deconvolution approaches. Then, the suitability and potential of the deconvolution procedure for retrieving the *f-k PSDF*s, with a special emphasis on the estimation of the Rayleigh phase velocities, are discussed by analysing two data sets collected using small arrays with different configurations in a test-site in the town of Potenza (Southern Italy).

2. Frequency-wavenumber methods

2.1 Beam-Forming and Maximum Likelihood Methods

In this section a short overview of the Beam-Forming Method (BFM) (Lacoss et al. 1969) and the Maximum Likelihood Method (MLM) (Capon, 1969) is provided. Both methods were originally proposed with the aim of detecting nuclear explosions using the seismic network LASA, which had a diameter of 200 km (Okada, 2003). For that reason, they were designed to single out the predominant seismic wave from a complex assemblage of other waves, irrespective of their nature (i.e., they work for both body and surface waves).
The estimate of the *f-k* spectra $EP_b(f,\mathrm{k})$ by the BFM is given by:

$$EP_b(f,\mathrm{k}) = \sum_{l,m=1}^{n} \phi_{lm} \exp\{i\mathrm{k}(\mathrm{X}_l - \mathrm{X}_m)\}, \qquad (1)$$

where f is the frequency, k the two-dimensional horizontal wavenumber vector, n the number of sensors. ϕ_{lm} is the estimate of the cross-power spectra between the lth and the mth data, and X_l and X_m are the coordinates of the lth and the mth sensors, respectively.
The MLM gives the estimate of the *f-k* spectra $EP_m(f,\mathrm{k})$ as:

$$EP_m(f,\mathrm{k}) = \left(\sum_{l,m=1}^{n} \phi_{lm}^{-1} \exp\{i\mathrm{k}(\mathrm{X}_l - \mathrm{X}_m)\} \right)^{-1}. \qquad (2)$$

With respect to the BFM, the inversion of the cross-power spectra complex matrix (ϕ_{lm}) is the only additional processing step. The inverse of ϕ_{lm} can be computed following standard numerical approaches, like performing the Singular Value Decomposition (SVD) (e.g., Press et al., 1992). Even if this step involves larger computational efforts, this method exhibits higher resolution than BFM in many cases.
Capon (1969) showed, in fact, that the resolving power of the MLM is higher than that of the BFM, mainly due to the adaptive nature of its wavenumber filter. However, the peak amplitude in the EP_m wave-number domain is tightly related to the signal-to-noise ratio, to the characteristics of the signal, and to the array geometry (Asten and Henstridge, 1984). In fact, MLM is more sensitive to measurement errors, for instance when the analyzed signal contains transients, and its higher resolving power with respect to BFM cannot be considered a general property (Okada, 2003).

The location of a peak occurring at coordinates k_{xo} and k_{yo} for a certain frequency f_o, in the EP_b and EP_m wave-number domain provides information about both the apparent propagation velocity, c_o, given by

$$c_o = \frac{2\pi f_o}{\sqrt{k_{xo}^2 + k_{yo}^2}}, \tag{3}$$

and the azimuth of the signal from the array (i.e., the back-azimuth), given by

$$\theta_o = \tan^{-1}\left(\frac{k_{xo}}{k_{yo}}\right). \tag{4}$$

An extensive description of these methods can be found in Horike (1985) and Okada (2003).

2.2 Array response function

The estimate EP_b and EP_m of the true P_b and P_m *f-k* spectra may be considered the convolution of the true functions with a frequency window function W_f and the wavenumber window functions W_B and W_M for the BFM and MLM, respectively (Lacoss *et al.*, 1969). The first window function W_f is the transfer function of the tapering function applied to the signal time windows (Kind et al., 2005). The function W_B, is referred differently by various authors (e.g. "*spatial window function*" by Lacoss et al., 1969, and "*beam-forming array response function*" by Capon, 1969), and hereafter is termed simply as the Array Response Function (ARF). The ARF depends only on the distribution of stations in the array, and for the wavenumber vector k_o has the form (Horike, 1985)

$$W_B(\mathrm{k},\mathrm{k}_o) = \frac{1}{n^2}\sum_{l,m=1}^{n} \exp\{i(\mathrm{k}-\mathrm{k}_o)(\mathrm{X}_l - \mathrm{X}_m)\}, \tag{5}$$

Simply speaking, it represents a kind of spatial filter for the wavefield.
The main advantage of the MLM with respect to the BFM involves the use of an improved wavenumber window W_M. That is, for a wavenumber k_0, this window function may be expressed in the form

$$W_M(f,\mathrm{k},\mathrm{k}_0) = \left|\sum_{j=1}^{n} A_j(f,\mathrm{k}_0)\right| W_B(\mathrm{k},\mathrm{k}_0), \tag{6}$$

where

$$A_j(f,\mathrm{k}_0) = \frac{\sum_{l=1}^{n} q_{jl}(f,\mathrm{k}_0)}{\sum_{j,l=1}^{n} q_{jl}(f,\mathrm{k}_0)}, \tag{7}$$

and where q_{jl} represents the elements of the cross-power spectral matrix. It is evident that W_M depends not only on the array configuration through the function W_B, but also on the quality (i.e., signal-to-noise ratio) of the data (Horike, 1985). In fact, the wavenumber response is modified by using the weights A_j (f, k_0), which depend directly on the elements $q_{lj}(f)$. In

practice, W_M allows the monochromatic plane wave traveling at a velocity corresponding to the wavenumber k_0 to pass undistorted, while it suppresses, in an optimum least-squares sense, the power of those waves traveling with velocities corresponding to wavenumbers other than k_0 (Capon, 1969). Or, in other words, coherent signals are associated with large weights of A_j and their energy is emphasized in the *f-k* spectrum. On the contrary, if the coherency is low, the weights A_j are small and the energy in the *f-k* spectrum is damped (Kind et al., 2005). This automatic change of the main-lobe and side-lobe structure for minimizing the leakage of power from the remote portion of the spectrum has a direct positive effect on the P_m function, and consequently on the following velocity analysis.

However, considering the dependence of W_M on W_B, it is clear that the array geometry is a factor having a strong influence on both EP_b and EP_m. In fact, similarly to every kind of filter, several large side lobes located around the major central peak can remain in the *f-k* spectra (Okada, 2003) and determine serious biases in the velocity and back-azimuth estimates. In particular, the side-lobe height and main-lobe width within W_B control the leakage of energy and resolution, respectively (Zywicki, 1999).

As a general criterion, the error in the velocity analysis due to the presence of spurious peaks in the *f-k* spectra may be reduced using distributions of sensors for which the array response approaches a two-dimensional δ-function. For that reason, it is considered good practice to undertake a preliminary evaluation of the array response when the survey is planned. Irregular configurations of even only a few sensors should be preferred, because they allow one to obtain a good compromise between a large aperture, which is necessary for sharp main peaks in the EP_b and EP_m, and small inter-sensor distances, which are needed for large aliasing periods (Kind et al., 2005).

3. Approaches to image deconvolution

Image deconvolution is commonly applied for mitigating the blurring effects introduced by the beam pattern of an antenna (termed '*image restoration problem*'). Following the general smearing (i.e. blurring) model with independent additive noise, a detected 2-D image $\boldsymbol{g}$ is given by

$$g = p * \delta + u \,, \tag{8}$$

where the symbol * denotes the 2-D convolution, $\boldsymbol{p}$ is the point-spread function (PSF), $\boldsymbol{\delta}$ is the original image, and $\boldsymbol{u}$ is noise. On the basis of what was discussed before, this problem is similar to the removal of smearing effects from the *f-k PSDF* matrix due to the array response functions, where the matrices $\boldsymbol{g}$, $\boldsymbol{\delta}$, and $\boldsymbol{p}$ correspond to the estimated *f-k PSDF*, the deconvolved *f-k PSDF*, and the ARF, respectively.

The image restoration problem consists of evaluating an estimate $E\boldsymbol{\delta}$ of the original image $\boldsymbol{\delta}$, being given the detected image $\boldsymbol{g}$ and the beam pattern $\boldsymbol{p}$ of the antenna. It is well known that this kind of problem is typically *ill-posed*, since the information provided by $\boldsymbol{g}$ and the PSF are insufficient to retrieve $\boldsymbol{\delta}$ univocally. Therefore, in this work we selected and applied two regularization methods widely used for image restoration problems: the *Tikhonov Regularization method* and the *Richardson-Lucy method*. In the following we provide only a brief discussion of these techniques. Interested readers are referred to Bertero and Boccacci (1998) for a more in-depth discussion of these and other techniques suitable for image restoration problems.

The *Tikhonov Regularization* (TR) is one of the simplest deconvolution methods. It consists of taking into account a penalty term proportional to the energy of the object (Engl *et al*, 1996). The basic equation of the *TR* can be written in the frequency domain as

$$E\hat{\Delta} = \frac{\hat{P}^*}{\left|\hat{P}\right|^2 + \mu}\hat{G}^2 \,, \tag{9}$$

where μ is a positive number, termed the regularization parameter, the star denotes the complex conjugate, and the capital symbols with the hat, $E\hat{\Delta}$, $\hat{G}$, and $\hat{P}$, denote the Discrete Fourier Transform (DFT) of the estimated image $E\boldsymbol{\delta}$, the detected image $\boldsymbol{g}$, and the PSF $\boldsymbol{p}$, respectively. The value of the regularization parameter μ determines the degree of filtering applied to the solution: the smoothness of the solution increases with increasing μ, reducing the effect of numerical instabilities but also the spatial resolution of the solution.

The *Richardson-Lucy Method* (RLM), proposed by Richardson (1972) and Lucy (1974) is the most frequently used, and also considered the most robust, deconvolution approach in astronomy for correcting radio-astronomical observations for the smoothing due to the beam pattern of the antenna. Essentially, the algorithm is based on maximizing the likelihood of the resulting deblurred image being an instance of the observed image under Poisson statistics. In

practice, the RLM algorithm consists of an iterative procedure that, for a given detected image and a certain PSF, allows the computation of the deblurred image (Bertero, and Boccacci, 2005). The RLM iterative procedure is given by:

$$E\delta^{(m+1)} = \frac{1}{\alpha} E\delta^{m} \left(A^{T} \frac{g}{AE\delta^{m}} \right), \tag{12}$$

where m is the number of iterations, $\boldsymbol{g}$ is the detected image and $E\boldsymbol{\delta}^{m}$ is the regularized solution at the *m-th* iteration. The inverse of the number of iterations acts as a regularization parameter, that is to say increasing the number of iterations diminishes the smoothness of the solution of the deconvolution problem, but produces noise amplification (Bertero and Boccacci, 2000). The image A is derived from the PSF, after having it zero padded at the boundaries. The matrix α is obtained from the sum of the elements of the 'columns' of the imaging matrix A (e.g. Bertero, and Boccacci, 2005). If the PSF is normalized, then α has a value approximately equal to 1 in the central region of the image, becoming smaller for pixels close to the boundaries, and with a decrease which depends on the behavior of the ARF (Bertero, and Boccacci, 2005). The iterations are generally stopped according to a pre-assigned criterion of convergence towards the maximum likelihood solution which varies depending on the application at hand.

In the following, during the application of the RLM algorithm, the matrix A will correspond to the ARF matrixes.

4. Test-site and data-set

Within the framework of the Italian DPC-INGV 2004-2006 projects, the town of Potenza (Southern Italy) was one of the test sites selected for preparing ground-motion scenarios and for comparing techniques for estimating site effects in urban environments. For this purpose, an area in the neighbouring village of Tito was selected by Parolai et al. (2007), and seismic noise recordings by 2D-arrays were carried out close to a 40 m deep borehole instrumented with two-sensors for the recording of teleseismic, regional, and local seismicity.

The Tito test site is located in the S. Loja Plain in southern Italy, along the axial zone of Southern Apennines (Figure 1). Previous geological studies (Pescatore et al., 1999) and geophysical investigations indicate that at the site a shallow layer of clay is inter-bedded with detritus and lenses of sand, and overlies a Flysch formation, which can be considered the engineering bedrock.

Parolai et al. (2007) deployed three seismometer micro-arrays close to the borehole, utilizing short-period sensors and digitizers with high dynamic range. Comparison of both S-wave velocity profiles obtained from passive investigations with those derived from down-hole measurements, and of empirical site responses with those calculated numerically from the S-wave velocity profiles obtained from the micro-array data, showed that seismic noise investigations with these arrays provide reliable results for the shallow subsoil structure and site effects characterization of a site.

For this work, we selected two arrays of the data-set of Parolai et al. (2007). The array geometries varied from a simple T-shape to a more complicated one (Figure 2).

Despite the constraints of the distribution of buildings in the area, both geometries were planned to provide a sufficient azimuth and inter-station distance coverage, allowing the retrieval of information about Rayleigh wave phase velocity in the frequency band between 2 and about 13 Hz.

For both arrays, the stations worked contemporaneously for more than 1 hour, recording noise at 500 s.p.s., which is adequate for the short inter-station distance considered. Every station was equipped with a 24 bit digitizer connected to a Mark L-4C-3D 1Hz sensor and GPS timing. For the analysis, the data recorded by each station of each array are divided into 60 s windows. A total of 44 non-overlapping windows are considered. Only the vertical component is analyzed. Recordings are corrected for the instrumental response considering the calibration parameters of each sensor.

Figure 2 shows the array geometries (top) and the respective ARFs (bottom) computed using eq. 5 for $\mathbf{k}_o$ equal to 0 and the ARF equal to W_B.

5. Results

5.1 Selection of the regularization method

Figure 3 and 4 present some of the results obtained by applying the two previously described regularization algorithms to the experimental *f-k PSDF* matrix evaluated at 3.5 and 13 Hz, respectively. These matrixes were estimated using the data-set of *Array 1* and the BFM. The ARF of Array 1 was previously shown in Figure 2c. The loci of points having *k* equal to the value of the most coherent energy pattern in the *f-k* images are depicted by a yellow circle. Thus, *f-k* maxima propagating with the same velocity of the maximum peak can be easily recognized. Moreover, in order to make the visualization of the deconvolution effects easier, a velocity section is drawn across the maximum of both the original and deconvolved matrixes, starting from the minimum velocity of 100 ms^{-1} until 3 times the velocity corresponding to the maximum. One of the aims of the velocity sections is to provide, through the maximum width, information about the uncertainty in the phase velocity estimation. The present scheme has been used for all the results presented in this work. Hereafter, we consider always the velocities corresponding to 0.8 of the peak maximum on both sides as representative of the uncertainties.

Both methods were applied to test a wide range of regularization parameter values. In particular, for the TR approach we tested μ values between 10 and 0.025. For the RLM we increased the number of iterations *m* from 5 to 20.

Figure 3 shows a summary of the test results for the frequency 3.5 Hz. The original *f-k PSDF* matrix (panel a) is characterized by a dominant coherent energy pattern smeared around the apparent phase velocity of 260 ms^{-1} and an azimuth of 176°. The velocity sections crossing the maximum peaks of the original *f-k* matrix are shown in panel 3b.
In order keep the number of lines reasonably small within panel 3b, we show the TR results only for μ equal to 1, 0.1, and 0.025 (i.e. from yellow to red). Similarly, the RLM results are shown for *m* equal to 5, 10, and 20 (i.e. from cyan to blue)
The *f-k* image regularized by RLM for *m* equal to 10 is shown in panel 3c, while panels (d, e, and f) show the *f-k* images regularized by TR for μ equal to 1, 0.1, and 0.025.

The velocity sections across the *f-k* peaks (panel 3b) show that the de-blurring improves significantly its resolution but the shape of the peak depends on the value of the regularization parameter. In particular, while the amplitude of the peak restored by regularizing the solution with LR is almost stable with respect to the number of iterations (panel 3b), the amplitude of the solution obtained with TR strongly depends on the selected value for μ. Figure 3 shows that the resolution and the amplitude of the main peak increase by decreasing the value of μ but at the price of amplifying the back-ground noise (panels 3b, d, e, and f). The results shown in Figure 3 suggest a stronger sensitivity of the TR approach to the signal-to-noise ratio.

The same analysis are performed for a frequency of 13 Hz, where the original matrix (panel 4a) is characterized by multiple peaks and a rather high background noise level. Even if the most energetic peak in the original *f-k* image is the one with an apparent phase velocity of 120 ms^{-1}, the comparison with the *f-k* images at lower and higher frequencies (not shown here, but through the dispersion curve shown in Figure 8) indicates that, unless unreliably large jumps in velocities are considered, the correct peak is that corresponding to plane waves propagating with an apparent phase velocity of about 200 ms^{-1} (panel a, and b). We believe that the presence of the large peak centered at 120 ms^{-1} is related to array response function bias effects.

The velocity sections in panel 4b and the *f-k* image in panel 4c indicate that the RLM allows, successfully, the removal of the array response function effects. In fact, in the RLM reconstruction the peaks corresponding to an apparent velocity of 180 ms^{-1} are less affected by numerical noise.
On the other hand, results shown in panels 4b, d, e, and f confirm that, when the deconvolution is regularized with TR, the *f-k* images are still affected by a higher level of noise. In particular, the reconstructed images are corrupted by the presence of several peaks, including those related to spatial aliasing effects. Furthermore, the peak related to the correct phase velocity is systematically smaller than those corresponding to an apparent velocity of 120 ms^{-1}. Moreover, we observe that with increasing the regularization, the background noise is amplified and the image is affected by a progressive, significant loss of resolution.

We are aware that both the case at hand and the performed tests do not cover all possible experimental situations. Nonetheless, our tests clearly indicate that, for the analyzed cases, the RLM provides results that show a better compromise between spatial resolution and stability of the solution with respect to noise amplification. Moreover, as expected from theory, the RLM preserves the positivity of the original image. Therefore, in the following sections we compare the normalized *f-k PSDF* matrixes, estimated using both the BFM and MLM, before and after the deconvolution for the ARF (hereafter 'Original Matrix' and 'Deconvolved Matrix', respectively) considering only the RLM algorithm.
In order to define a suitable number of iteration for applying the RLM algorithm to the case at hand, we repeated the procedure varying this parameter from 5 until a maximum number of iterations equal to 1000. Figure (5) shows the normalized *f-k PSDF* matrixes for the frequency of 13 Hz for some of the experiments. In agreement with theory (e.g. among the others, Bertero and Boccacci, 2000), we observe that with the increase of the number of iterations the noise in the figure is strongly amplified (Figure 5, panels for a number of iterations equal to 100 and 1000), and the main peaks are not related anymore with a reliable Rayleigh wave phase velocity. These observations reflect the fact that, despite the RLM algorithm provides a sequence converging towards the maximum likelihood solution, numerical simulations indicate that it has a semi-convergence property only (Bertero and Boccacci, 2000), and thus, when the number of iteration is too high the algorithm is blinded from noise.
So as other iterative deconvolution procedures, being in our case the 'true' solution unknown, we cannot use any objective criteria for defying the optimal criteria for stopping the iterations.

Therefore, we selected a number of iterations that represent a good compromise between the spatial resolution and the stability of the solution. In particular, we observed that a number of iterations equal to 10 guarantee, for the whole range of frequencies of interest, a good quality of the reconstructed images, allowing a clear identification of both the main maxima related to the Rayleigh wave traveling across the array, and also of those maxima, with equivalent velocity, that related to other seismic noise sources.
For each *f-k* image, which is computed starting from the stack of 44 non-overlapping signal windows, the maximum is selected and assumed to correspond to the Rayleigh wave phase velocity.

5.2 Array 1

Figure 6 shows the results of the *f-k* BFM analysis for the frequency 3 Hz (panels 6a), 5 Hz (panels 6b), and 13 Hz (panels 6c). Due to the rather limited soft sedimentary cover thickness, the frequency 3 Hz is already related to a wavelength comparable with the maximum dimension of the array, that is, the maximum is located in the proximity of the center plot (panel 6a - Original Matrix). However, it is worth noting that the maximum in the Deconvolved Matrix (panel 6a - Richardson-Lucy Method) has definitely a sharper shape. The variation of both the location and shape of the maximum after the deconvolution are clearly observable in the velocity sections (panel 6a - Velocity Section). These results show that the deconvolution operation allows a well defined maximum shape, and therefore a more accurate phase velocity estimation to be obtained. Moreover, it is worth noting that a remarkable decrease in the uncertainty occurs, especially towards the higher velocities, where, as observed by Okada (2003), there are significant degeneration effects hampering the *f-k* phase velocity estimations.
Similar results are shown for the frequency 5 Hz (panels 6b). Moreover, in this case, by the reduction of blurring, obtained thanks to the deconvolution, the capability to distinguish the contribution of different sources to the wavefield is improved (panel 6b - Richardson-Lucy Method).
In the higher-frequency range, i.e. 13 Hz (panels c), correcting the *f-k PSDF* by the ARF allows a reduction in the bias effects due to the spatial aliasing. In fact, panel 6c (Richardson-Lucy Method) shows that for this frequency, where the wavelength is comparable to the average inter-station distance and bias effects related to the spatial aliasing start to be significant, the *f-k* plot for the Original Matrix is affected by a higher level of noise. The velocity section extracted for the original *f-k* image presents two distinct peak, with the higher at a velocity of 120 ms^{-1} (panel 6c - Velocity Section). When the ARF contribution is removed, the level of noise in the *f-k* plot is considerably decreased (panel 5c - Richardson-Lucy Method), while panel 6c (Velocity Section) shows that after the deconvolution, the peak with a velocity of 120 ms^{-1} has an amplitude halved with respect to its original value. On the other hand, the peak related to the higher phase velocity (180 ms^{-1}) becomes sharper, has a smaller level of uncertainty due to its reduced width, and does not vary in amplitude.

Despite the well known higher resolution of the MLM over the BFM, the deconvolution for the ARF also improves the MLM analysis. Figure 7 shows the results obtained from applying the RLM regularization to the MLM *f-k* images for the same frequencies as the BFM analysis. Similarly to the previous analysis, we observe for the corrected *f-k* images a general reduction in the smearing that leads to a decrease in the uncertainty in the phase velocity estimation and to the increase of sharpness in the peak. Moreover, a considerable decrease in amplitude of the noisy peak is particularly important for the higher frequencies. In fact, the deconvolution for the ARF allows us to decrease the amplitude of the alias peak at a lower velocity (i.e. about 120 ms^{-1}) (panel 7c - Velocity Section). Being comparable to the phase velocity values of the neighboring frequencies (showed in the following Figure 8), the peak at the higher velocity is considered the most reliable one.
As shown in Figures 6 and 7, the capability to discriminate different sources of seismic noise is improved by removing the array response, which makes it also easier to discriminate and study the different phases in the wavefield.
Finally, Figure 8 shows a comparison of the Rayleigh wave dispersion curves obtained for the BFM and MLM, with and without the deconvolution for the ARF, together with the relevant uncertainties. The main effects of the deconvolution are a general decrease in the level of uncertainty related to the peak width in the *f-k* plots. This is particularly evident in the low frequency range, i.e. from about 2 Hz to about 6 Hz. Moreover, in the case of the BFM, we also observe a slight decrease in the phase velocity estimates. Although for most of the frequency range analyzed the phase velocities are correctly estimated without correcting the *f-k PSDF* for the ARF, we note that at high frequencies, the negative effects of the spatial aliasing, which hampers both the BFM and MLM curves over 10 Hz, are reduced and estimated phase velocity values are coherent with those of other frequencies.

5.3 Array 2

In the following we show the result for the frequencies 3 Hz and 10 Hz after having corrected for the array response using the RLM
As shown in Figure 2, the sensor configuration of the second array is quite simple and regular compared with that of the first one. For this reason, the ARF for the second array is characterized by high secondary peaks along the two *f-k* plot axes. The general effect of such an array configuration is a higher level of blurring noise in the *f-k* plots for both the BFM and MLM (Figure 9) with respect to that of the first array.
The deconvolution for the ARF shows once again the capability to considerably increase the signal-to-noise ratio of the *f-k* images (e.g. defined qualitatively as the ratio between the peak amplitude and the average background values), allowing a better selection of the high energy maxima, together with a lower level of uncertainty.
Figure 9 presents the *f-k* images before and after the deconvolution for the ARF for both the BFM and MLM. Despite the important role of the deconvolution for the ARF, the improvements in the dispersion curve trends are in this case quite modest (Figure 10). In fact, even if the level of uncertainty decreases considerably, the phase velocity trend with the increase in frequency is still irregular both for the BFM and MLM. This means that the effect

of poor geometry is dominant with respect to the improvement that can be obtained by correcting the *f-k PSDF* for the ARF.

6. Conclusions

The frequency-wavenumber images computed for small-size arrays (radius of the order of a few tens of meters) are blurred by the array transfer function and corrupted by noise. In particular, the limited number of deployed stations typically available during seismic surveys produces significant spread in the transfer function, while both spatial aliasing effects and incoherent energy arrivals decrease the signal-to-noise ratio of the data, especially at higher frequencies. Analyzing experimental seismic noise data-sets recorded with 2D-arrays of sensors, we showed that the deconvolution of the array transfer function in the *f-k* analysis allows us to obtain several improvements when either the beam-forming or the maximum-likelihood methods are used, although the de-blurring approach can also be applied to other *f-k* analysis methods.
The correction of *f-k* images by deconvolution with the ARF is an ill-posed problem that requires regularization. The performance of two well known regularization approaches (i.e. the Tikhonov and Richardson-Lucy methods) has been investigated considering two different array geometries. The results showed that the Richardson-Lucy method provides a better compromise between the resolution of the main features in the restored image and stability against amplification of error. In particular, the amplitude of the peak relevant to the plane wave propagating with the correct velocity through the array is weakly dependent on the regularization parameters and the solution preserves the positivity of the original *f-k* image, as expected from theory.

The results obtained with an irregular configuration of stations (*Array 1*) indicate that removing the array response function improves the resolution of the *f-k* images. Moreover, it has been shown that the main advantage related to the peak shape improvement is a general reduction in the level of uncertainty associated with the phase velocity. Another aspect related to the improved shape of the maxima in the *f-k* plots is that after the deconvolution, they appear to be much better separated and more easily identifiable from the others. This will contribute to obtaining greater precision in wavefield and source distribution studies.
Furthermore, in the case of the high frequency range, due to the wavelength and the array size characteristics, spatial aliasing effects cause a high level of noise in the *f-k* plots, hampering the analysis and leading user to select the incorrect *f-k* maxima, and therefore, wrong phase velocity values. However, we have showed that the deconvolution for the array response function can also be effective in these cases, allowing both the reduction of the noise and the selection of the correct *f-k* maxima and phase velocities.
Finally, it must be noted that, as indicated from the analysis (*Array 2*), the deconvolution for the array response function is less effective in retrieving an accurate phase velocity dispersion curve for cases of unfavorable array geometries (i.e. *f-k* images computed for a more regular

configuration of stations, as for example, the cases where the geometry is strongly constrained by the distribution of buildings).

In conclusion, in analogy to the correction for the instrumental response of seismological data, we think that the correction of the array transfer function should become a standard procedure during the frequency-wavenumber analysis of seismic noise array data. For this purpose, we showed that the Richardson-Lucy method is an effective and robust tool for the de-blurring of *f-k* images from the array response function.

Acknowledgements.
We thank K Fleming, who kindly improved the English. Some of the figures were generated using GMT (Wessel and Smith, 1991). Thanks to R. Milkereit for assistance with figures drawing. Instruments were provided by the Geophysical Instrumental Pool, Potsdam (GIPP).

REFERENCES

Aki, K., 1957. Space and time spectra of stationary stochastic waves, with special reference to microtremors, *Bull. Earthq. Res. Inst.*, 35, 415-456.

Asten, M.W., and Henstridge, J.D., 1984. Array estimators and use of microseisms for reconnaissance of sedimentary basins. *Geophysics*, 49, 1828,1837.

Bertero, M., and Boccacci, P., 1998. Introduction to Inverse Problems in Imaging, *IOP Publishing*, Bristol.

Bertero, M., and Boccacci, P., 2000. Image restoration methods for the Large Binocular Telescope (LBT), *Astron. Astrophys. Suppl. Ser.* 147, 323-333

Bertero, M., and Boccacci, P., 2005. A simple method for the reduction of boundary effects in the Richardson-Lucy approach to image deconvolution, *Astron. Astrophys*. 437, 369-374.

Birtill, J.W., and Whiteway, F.E., 1965. The application of phased arrays to the analysis of seismic body waves, *Philos. Trans. R. Soc. London*, Ser. A, 258, 421-493.

Capon, J., Greenfield, R.J., Kolker, R.J., 1967. Multidimensional Maximum-Likelihood Processing of a Large Aperture Seismic Array, *Proceedings of the IEEE*, 55, .2, 192-211.

Capon, J., 1969. High-resolution frequency-wavenumber spectrum analysis, *Proc. IEEE*, 57, 8, 1408-1418.

Carpenter, E.W., 1965. A historical review of seismometer array development, *Proc. IEEE*, 53, 1816-1833.

Douglas, A., 2002. Seismometer arrays – Their use in earthquake and test ban seismology, in *Handbook of Earthquake and Engineering Seismology*, edited by P. Jennings, H. Kanamori, and W. Lee, 357-367, Academic, San Diego, Calif.

Engl, H.W., Hanke, M., Neubauer, A., 1996. Regularization of Inverse Problmes, Kluwer, Dordrecht.

Frosch, R.A., and Green, P.E., 1966. The concept of the large aperture seismic array, *Proc. R. Soc. London*, Ser. A, 290, 368-384.

Halldorsson, B., Sigbjornsson, R., and Schweitzer, J., 2009. *Journal of Seismology*, 13, 173-178.

Harjes, H.P., and Henger, M., 1973. Array-Seismologie, *Z. Geophs.*, 39, 865-905.

Haubrich, R.A., 1968. Array design, *Bull. Seism. Soc. Am.*, 58, 977-991.

Horike, M., 1985. Inversion of phase velocity of long period micro tremors to the S-wave-velocity structure down to the basement in urbanized areas, *J. Phys. Earth*, 33, 59-96.

Hough, S.E., Seeber, L., Rovelli, A., Malagnini, L., DeCesare, A., Selvaggi, G., and Lerner-Lam, A., 1992. Ambient noise and weak motion excitation of sediment resonances: results from the Tiber Valley, Italy, *Bull. Seism. Soc. Am.*, 82, 1186-1205.

Kárason, H., and van der Hilst, R.D., 2001. Tomographic imaging of the lowermost mantle with differential times of refracted and diffracted core phases (PKP, P_{diff}), *J. Geophys. Res.*, 106, 6569-6587.

Kind, F., Fäh, D., Giardini, D., 2005. Array measurements of S-wave velocities from ambient vibrations, *Geophysical Journal International*, 160, 114-126.

Krűger, F., Baumann, M., Scherbaum, F., and Weber, M., 2001. Mid mantle scatterers near the Mariana slab detected with a double array method, *Geophys. Res. Lett.*, 28, 667-670.

Lacoss, R.T., Kelly, E.J., Toksöz, M.N., 1969. Estimation of seismic noise structure using arrays, *Geophysics*, 34, 21-38.

Lucy, L.B., 1974. An iterative technique for the rectification of observed distribution, *The Astronomical Journal*, 79,.6,.745-754.

Mykkeltveit, S., Astebol, K., Doornbos, D.J., and Husebye, E.S., 1983. Seismic array configuration optimization, *Bull. Seismol. Soc. Am.*, 73, 173-186.

Nishida, K., Kawakatsu, H., Fukao, Y., and Obara, K., 2008. Background Love and Rayleigh waves simultaneously generated at the Pacific Ocean floors, *Geophys. Res. Lett.*, 35, L16307-L16312.

Ohori, M., Nobata, A., and Wakamatsu, K., 2002. A comparison of ESAC and FK methods of estimating phase velocity using arbitrarily shaped microtremor analysis, *Bull. Seism. Soc. Am.*, 92, 2323-2332.

Okada, H., 2003. The Microtremor Survey Method. Geophys, Monograph Series, SEG, 129 pp.

Parolai, S., Picozzi, M., Richwalski, S.M., and Milkereit C., 2005. Joint inversion of phase velocity dispersion and H/V ratio curves from seismic noise recordings using a genetic algorithm, considering higher modes, *Geoph. Res. Lett.*, 32, doi: 10.1029/2004GL021115.

Parolai, S., Mucciarelli, M., Gallipoli, M.R., Richwalski, S.M., and Strollo, S., 2007. Comparison of Empirical and Numerical Site Responses at the Tito Test Site, Southern Italy, *Bull. Seism. Soc. Am.*, 97, 1413-1431.

Pescatore, T., Renda, P., Schiattarella, M., and Tramutoli, M., 1999. Stratigraphic and structural relationships between Mso-Cenozoic Lagonegro basin and coeval carbonate platforms in southern Apennines, Italy, *Tectonophysics*, 315, 269-286.

Press, W.H., Teukolsky, S.A., Vetterling, W.T., Flannery, B.P., 1992. Numerical Recipes in Fortran, second edition, Cambridge University Press.

Richardson, W.H., 1972. Bayesian-Based Iterative Method of Image Restoration, *Journal of the Optical Society of America*, 62 (1), 55–59.

Ritter, J.R.R., Jordan, M., Christensen, U., and Achauer, U., 2001. A mantle plume below the Eifel volcanic fields, Germany, *Earth Planet. Sci. Lett.*, 186, 7-14.

Rost, S., and Thomas, C., 2002. Array Seismology: Methods and Applications, *Reviews of Geophysics*, 40, 3. 1-27.

Rost, S., and Thomas, C., 2009. Improving Seismic Resolution Through Array Processing Techniques, *Surv. Geophys*., 30, 271-299.

Scherbaum, F., Hinzen, K.-G., and Ohrnberger, M., 2003. Determination of shallow shear-wave velocity profiles in Cologne, Germany area using ambient vibrations, *Geophys. J. Int.*, 152, 597-612.

Somers, H., and Manchee, E. B., 1966. Selectivity of the Yellowknife seismic array, *Geophys. J. R. astr. Soc.*, 10, 401-412.

Wathelet, M., Jongmans, D., and Ohrnberger, M., 2005. Direct Inversion of Spatial Autocorrelation Curves with the Neighborhood Algorithm, *Bull. Seism. Soc. Am.*, 95, 1787-1800.

Wessel P and Smith W H F 1991 Free software helps map and display data. *EOS (AGU)*, 72 (41), 441, 445-446.

Whiteway, F.E., 1966. The use of arrays for earthquake seismology, *Proc. R. Soc. London*, Ser. A, 290, 328-348.

Zywicki, D.J., 1999. Advanced Signal Processing Methods Applied to Engineering Analysis of Seismic Surface Waves. PhD thesis at Georgia Institute of Technology.

Figure Caption

Figure 1: Location of the Tito test site.

Figure 2: *Top*. 2D-array configurations (*a) Array 1*, *b) Array 2*). *Bottom*: 2D-array response functions (*c)* for *Array 1*, *d)* for *Array 2*).

Figure 3: Comparison of different image deconvolution approaches. *a)* Input Matrix normalized to its maximum for the frequency 3.5 Hz. *b)* Velocity sections for the original matrix (*black* line), for different μ values (i.e. *yellow line* when equal to 1, *orange line e* when equal to 0.1, and *red line* when equal to 0.025) using the *Tikhonov Regularization*, TR, and for different *m* values (i.e. *cyan line* when equal to 5, *light blue line* when equal to 10, and *dark blue line* when equal to 20) for the *Richardson-Lucy Method*, RLM. *c*) deconvolved matrix by *Richardson-Lucy Method*, RLM, for *m* equal to 10. *d*) Deconvolved matrix by *Tikhonov Regularization*, TR, for μ equal to 1. *e*) Same as *d*), but for μ equal to 0.1. *f*) Same as *d*), but for μ equal to 0.025.

Figure 4: Same as Figure 3, but for 13 Hz.

Figure 5: Comparison of different normalized *f-k PSDF* matrixes for the frequency of 13 Hz, and number of iterations when applying the RLM algorithm. The black arrows indicate the location of the main peak.

Figure 6: Results of the *f-k* analysis for *Array 1* data-set using the BFM. *a*) Panels for the frequency 3Hz. Original Matrix (panel *a - left*), Richardson-Lucy Method Matrix (panel *a - middle*), Velocity sections for the Input Matrix (*red*) and for the Deconvolved Matrix (*green*) (panel *a – right*). *b*) Same as a), but for frequency 5 Hz. *c*) Same as a), but for frequency 13 Hz. Yellow dots indicate the position of the maximum used to estimate the phase velocity. The yellow circle joins points with the same *k* value.

Figure 7: Same as Figure 5, but using the MLM.

Figure 8: *a)* BFM dispersion curves for *Array 1* obtained by the selection of apparent phase velocity values from the Original Matrix (*red line*) and Deconvolved Matrix (*black line*), together with the estimated level of uncertainty (*dotted lines*). *b)* Same as *a)* but for the MLM.

Figure 9: Same as Figure 5, but for *Array 2*. *a*) Frequency 3 Hz using BFM. *b*) Frequency 10 Hz using BFM. *c*) Same as *a*), but using MLM. *d*) Same as *b*), but using MLM.

Figure 10: Same as Figure 7, but for *Array 2*.

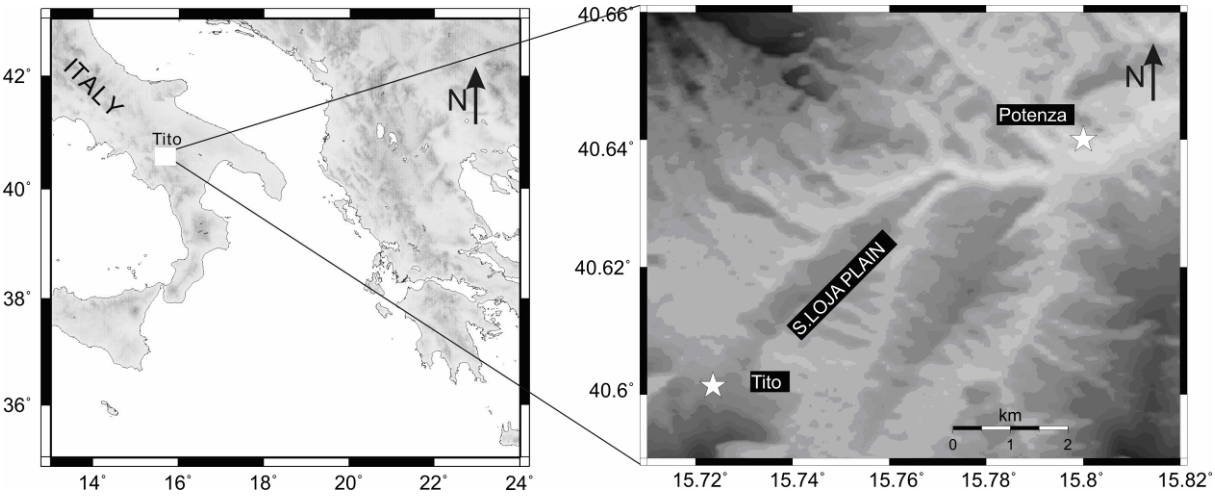
ITALY
Tito
N
42°
40°
38°
36°
14°
16°
18°
20°
22°
24°
40.66°
40.64°
40.62°
40.6°
Potenza
S.LOJA PLAIN
Tito
km
0
1
2
15.72°
15.74°
15.76°
15.78°
15.8°
15.82°

Figure 1

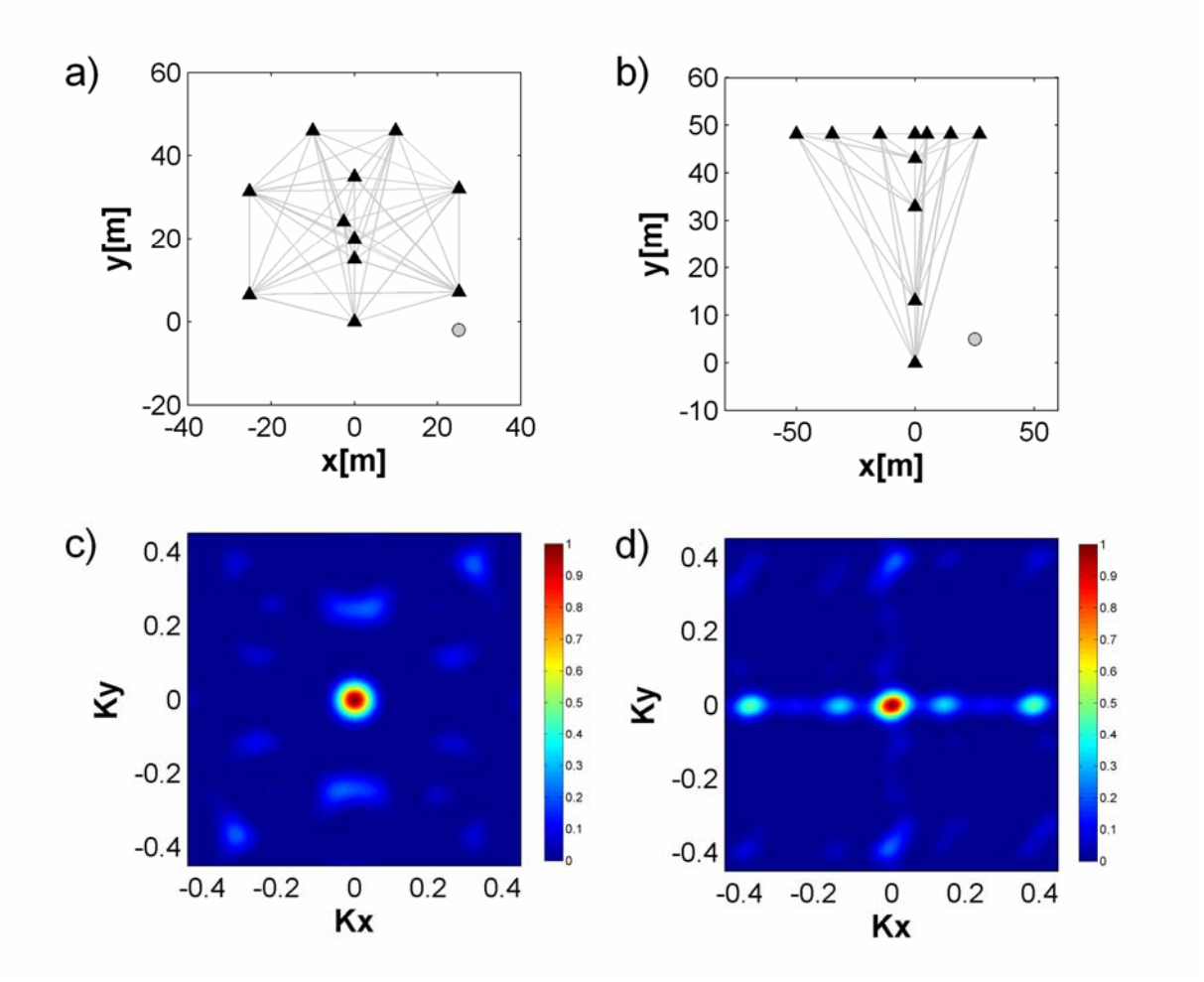

Figure 2

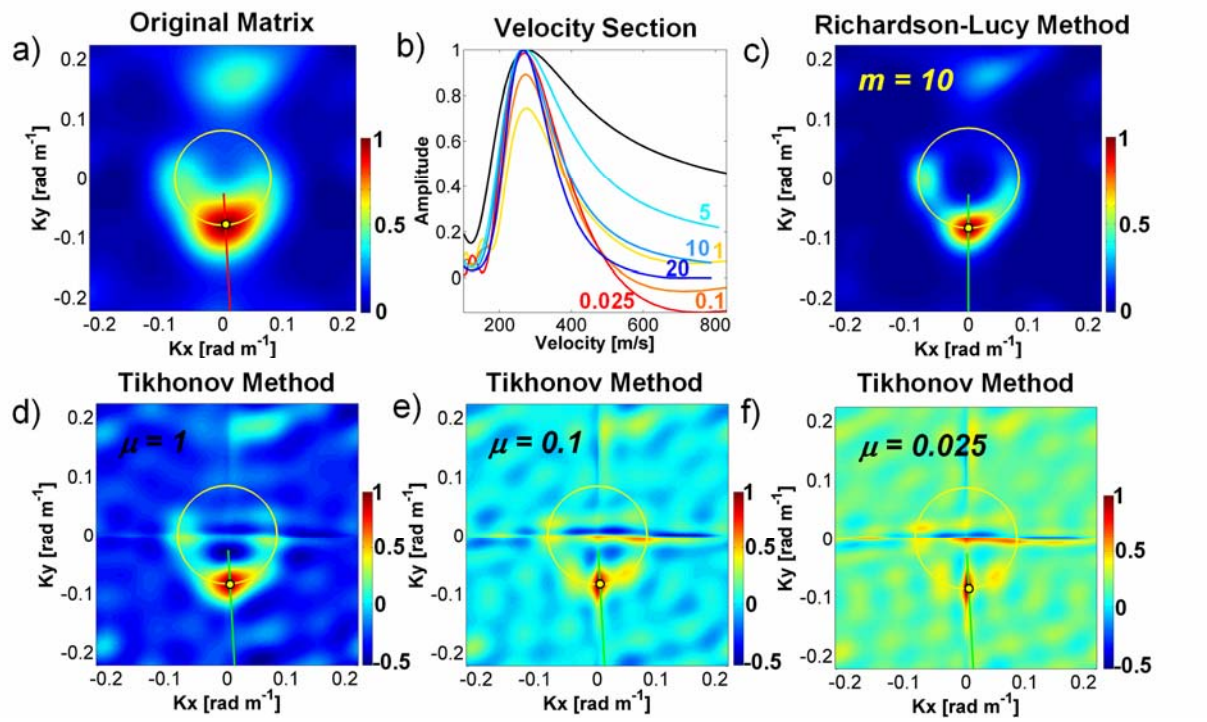
a)
Original Matrix
Ky [rad m-1]
Kx [rad m-1]
b)
Velocity Section
Amplitude
Velocity [m/s]
5
10
1
20
0.025
0.1
c)
Richardson-Lucy Method
m = 10
d)
Tikhonov Method
μ = 1
e)
Tikhonov Method
μ = 0.1
f)
Tikhonov Method
μ = 0.025

Figure 3

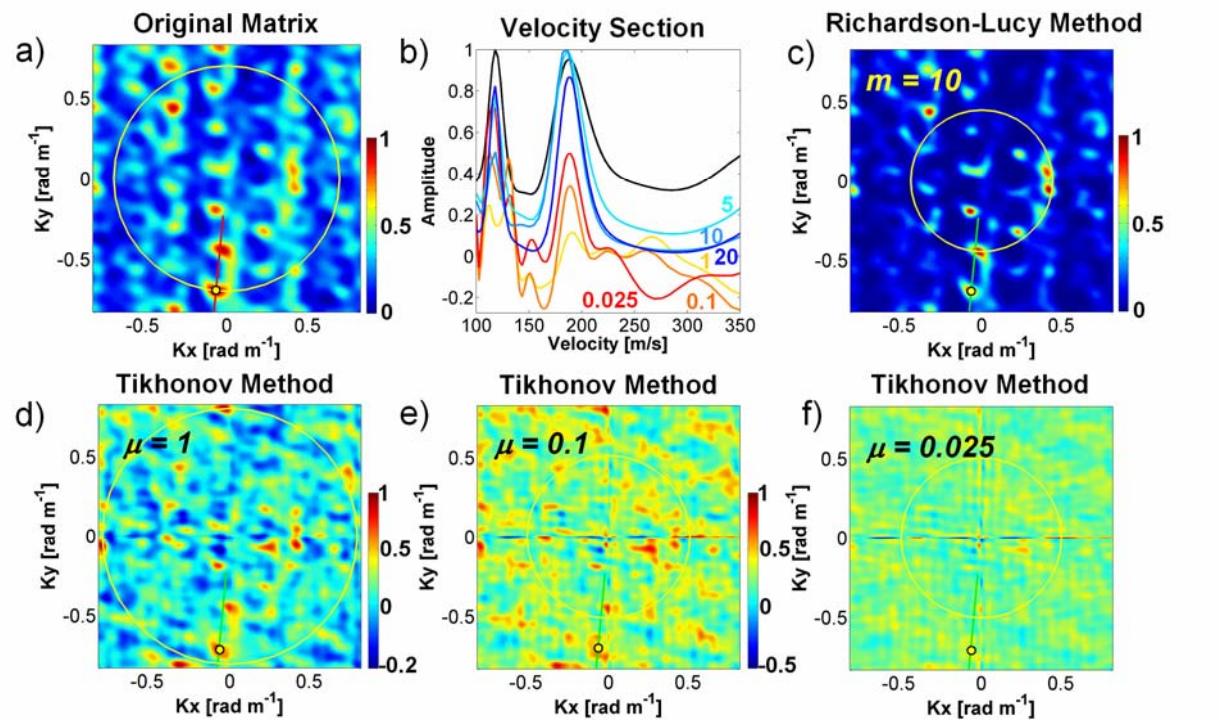
a)
Original Matrix
Ky [rad m-1]
Kx [rad m-1]
b)
Velocity Section
Amplitude
Velocity [m/s]
5
10
1
20
0.025
0.1
c)
Richardson-Lucy Method
m = 10
d)
Tikhonov Method
μ = 1
e)
Tikhonov Method
μ = 0.1
f)
Tikhonov Method
μ = 0.025

Figure 4

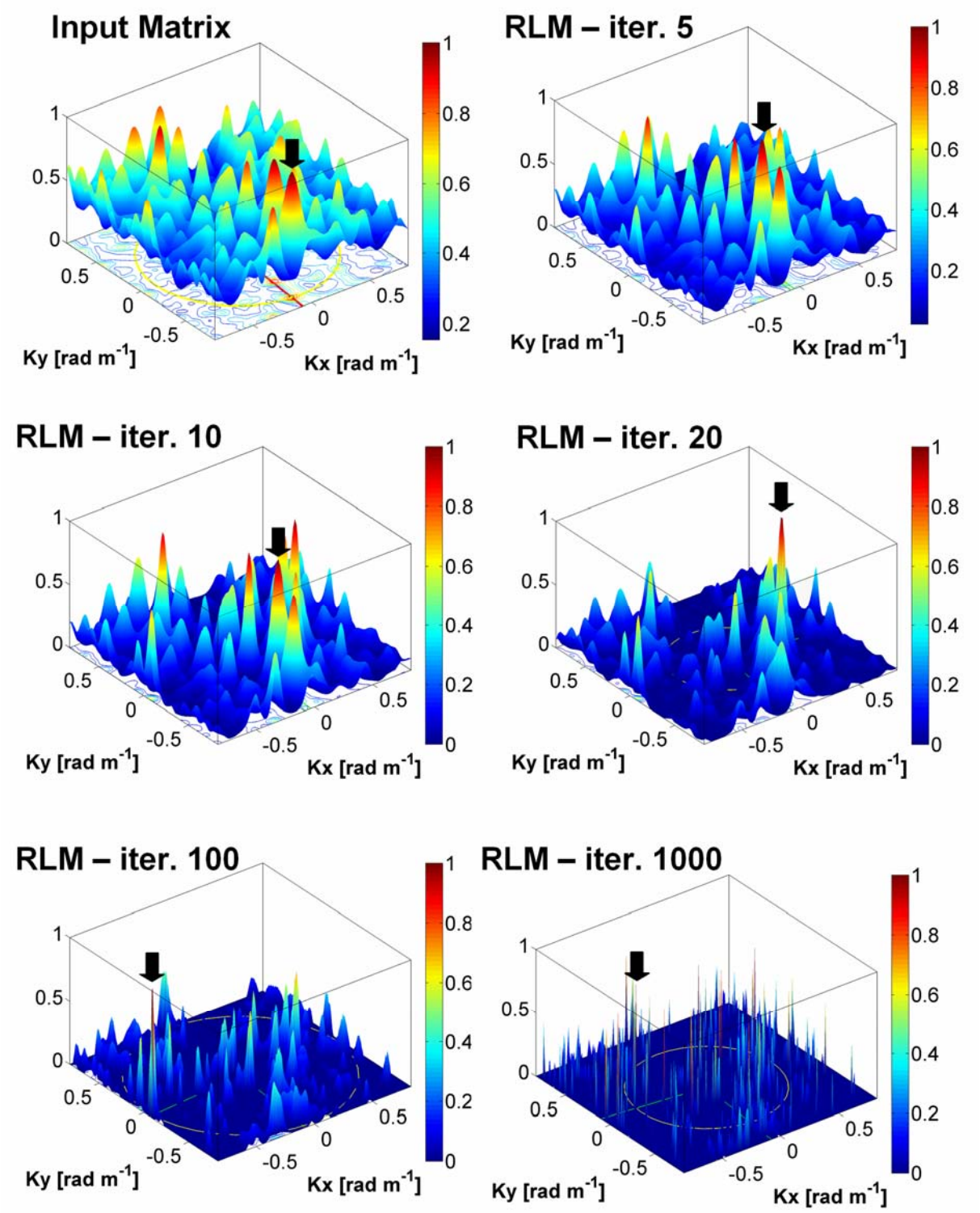
Input Matrix
RLM – iter. 5
RLM – iter. 10
RLM – iter. 20
RLM – iter. 100
RLM – iter. 1000
Ky [rad m-1]
Kx [rad m-1]

Figure 5

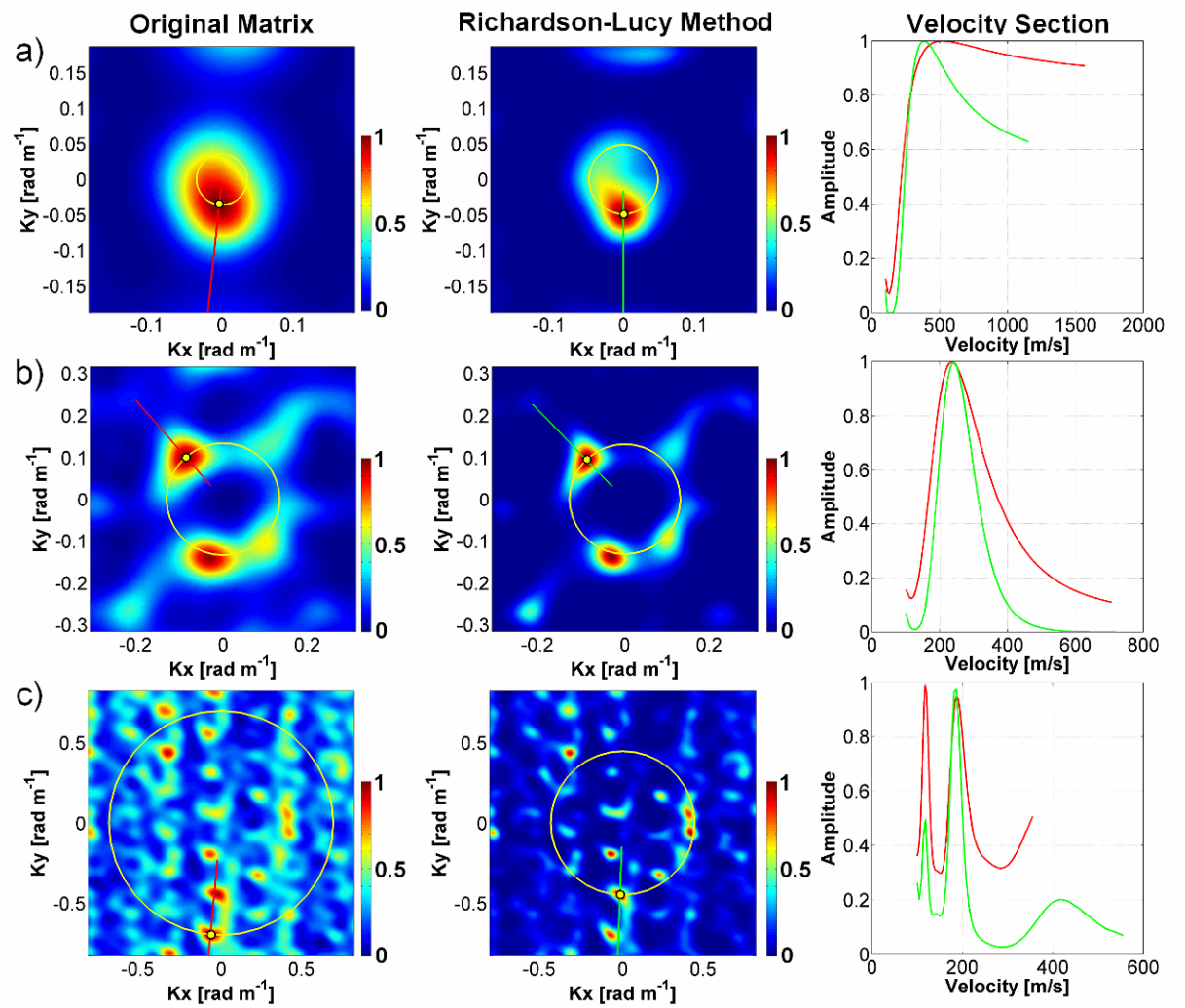
Original Matrix
Richardson-Lucy Method
Velocity Section
a)
b)
c)
Ky [rad m-1]
Kx [rad m-1]
Amplitude
Velocity [m/s]

Figure 6

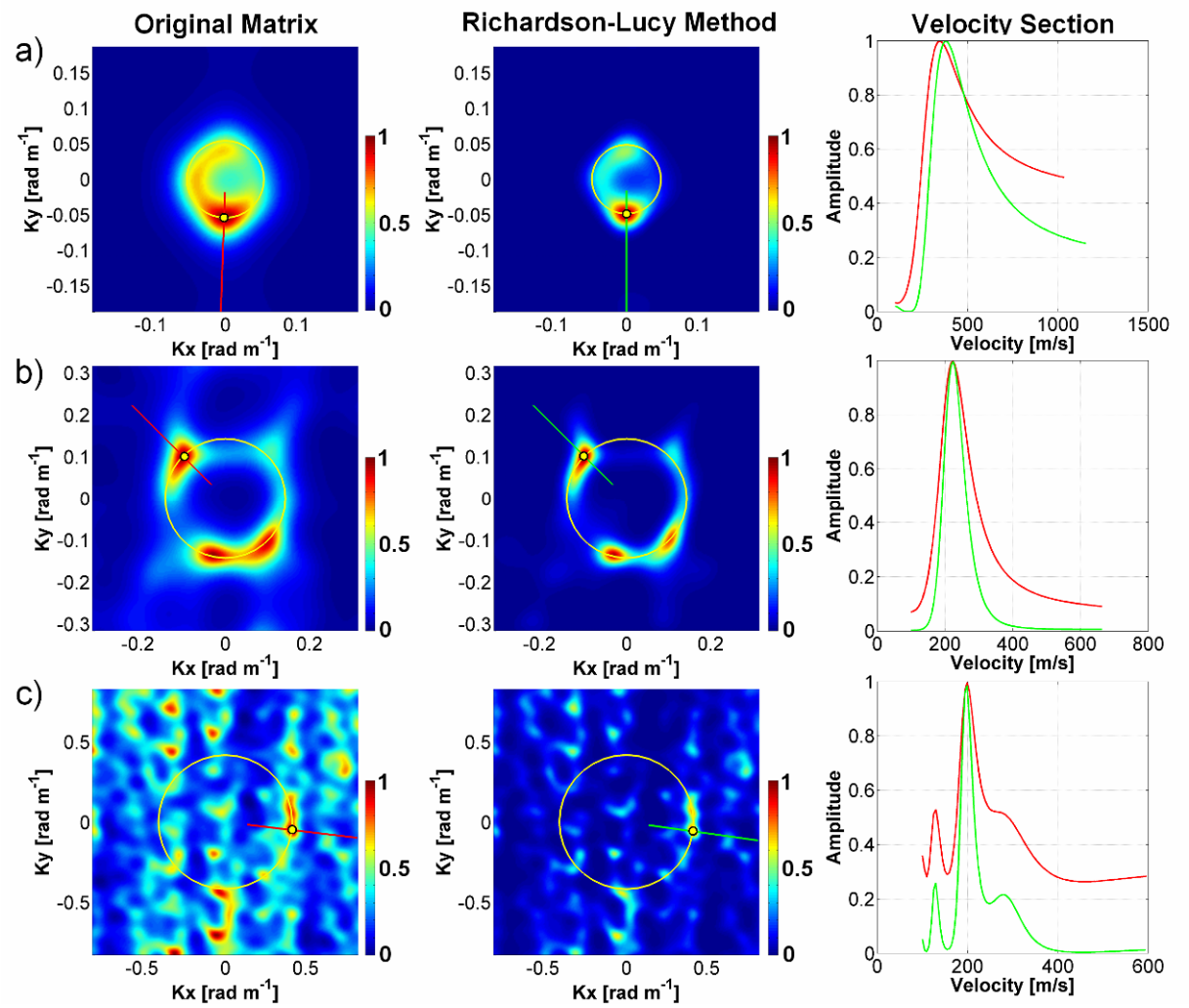
Original Matrix
Richardson-Lucy Method
Velocity Section
a)
b)
c)
Ky [rad m-1]
Kx [rad m-1]
Amplitude
Velocity [m/s]

Figure 7

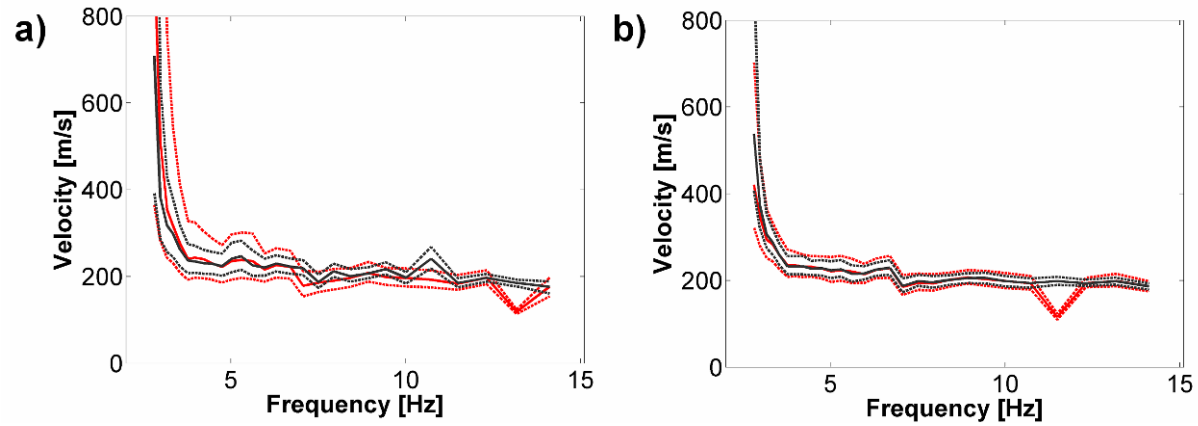

Figure 8

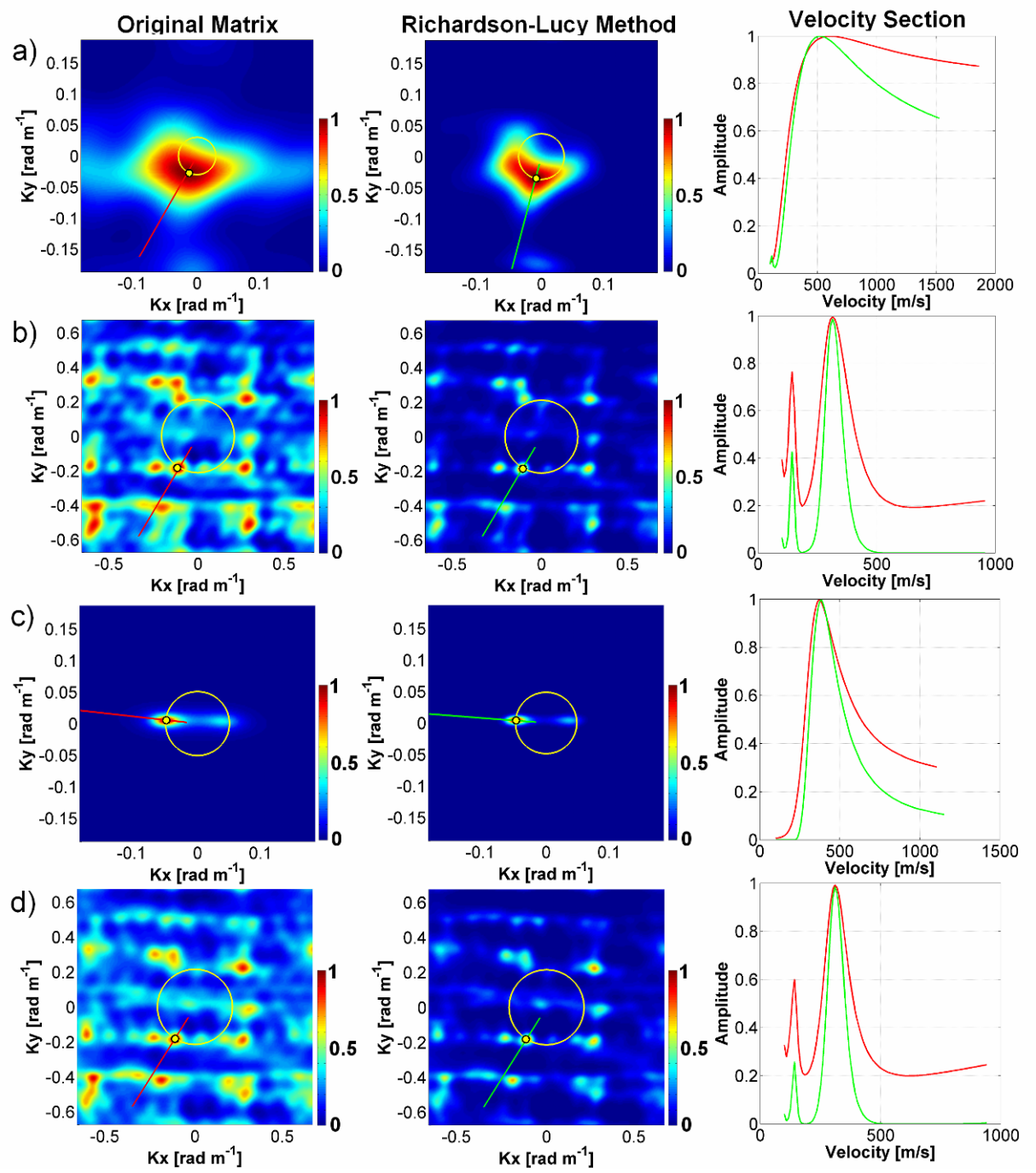
Original Matrix
Richardson-Lucy Method
Velocity Section
a)
b)
c)
d)
Ky [rad m-1]
Kx [rad m-1]
Amplitude
Velocity [m/s]

Figure 9

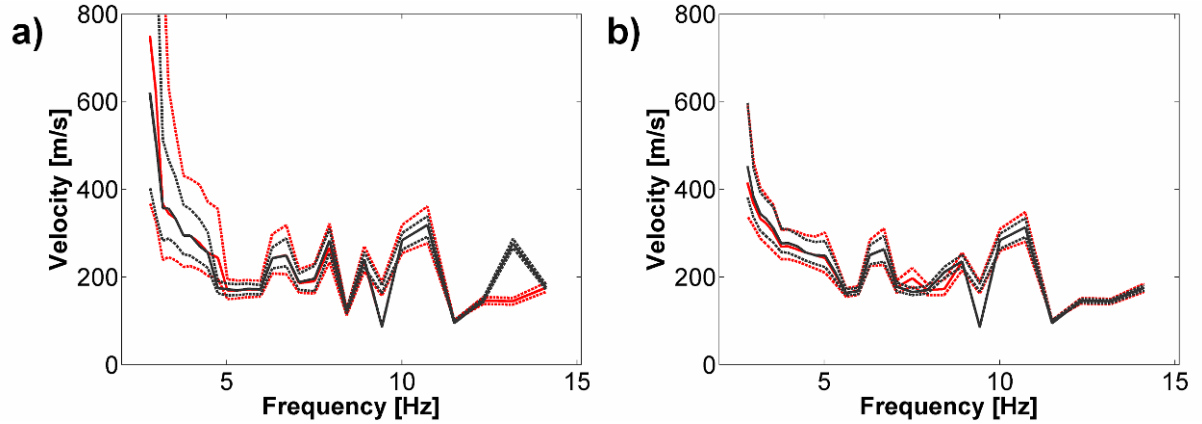

Figure 10